Biomedical Microdevices (2019) 21: 41
https://doi.org/10.1007/s10544-019-0398-5

A tissue chamber chip for assessing nanoparticle mobility in the extravascular space

Valeria Lusi[1,2] · Thomas L. Moore[1] · Federica Laurino[1,3] · Alessandro Coclite[1] · Rui Perreira[1] · Miguel Ferreira[1] · Ilaria Rizzuti[1] · Roberto Palomba[1] · Paolo Zunino[3] · Marti Duocastella[4] · Shoshy Mizrahy[1,5] · Dan Peer[5] · Paolo Decuzzi[1]

Published online: 6 April 2019

Abstract

Although a plethora of nanoparticle configurations have been proposed over the past 10 years, the uniform and deep penetration of systemically injected nanomedicines into the diseased tissue stays as a major biological barrier. Here, a 'Tissue Chamber' chip is designed and fabricated to study the extravascular transport of small molecules and nanoparticles. The chamber comprises a collagen slab, deposited within a PDMS mold, and an 800 μm channel for the injection of the working solution. Through fluorescent microscopy, the dynamics of molecules and nanoparticles was estimated within the gel, under different operating conditions. Diffusion coefficients were derived from the analysis of the particle mean square displacements (MSD). For validating the experimental apparatus and the protocol for data analysis, the diffusion D of FITC-Dextran molecules of 4, 40 and 250 kDa was first quantified. As expected, D reduces with the molecular weight of the dextran molecules. The MSD-derived diffusion coefficients were in good agreement with values derived via fluorescence recovery after photobleaching (FRAP), an alternative technique that solely applies to small molecules. Then, the transport of six nanoparticles with similar hydrodynamic diameters (~ 200 nm) and different surface chemistries was quantified. Surface PEGylation was confirmed to favor the diffusion of nanoparticles within the collagen slab, whereas the surface decoration with hyaluronic acid (HA) chains reduced nanoparticle mobility in a way proportional to the HA molecular weight. To assess further the generality of the proposed approach, the diffusion of the six nanoparticles was also tested in freshly excised brain tissue slices. In these ex vivo experiments, the diffusion coefficients were 5-orders of magnitude smaller than for the Tissue Chamber chip. This was mostly ascribed to the lack of a cellular component in the chip. However, the trends documented for PEGylated and HA-coated nanoparticles *in vitro* were also confirmed ex vivo. This work demonstrates that the Tissue Chamber chip can be employed to effectively and efficiently test the extravascular transport of nanomedicines while minimizing the use of animals.

Keywords Nanoparticle transport · Nanomedicine · Tissue chamber

Electronic supplementary material The online version of this article (https://doi.org/10.1007/s10544-019-0398-5) contains supplementary material, which is available to authorized users.

✉ Paolo Decuzzi
paolo.decuzzi@iit.it

[1] Laboratory of Nanotechnology for Precision Medicine, Italian Institute of Technology, Via Morego 30, 16163 Genoa, Italy

[2] DIBRIS, University of Genova, Via Opera Pia 13, 16145 Genoa, Italy

[3] MOX, Department of Mathematics, Politecnico di Milano, Piazza Leonardo da Vinci 32, 20133 Milan, Italy

[4] Nanophysics, Italian Institute of Technology, Via Morego 30, 16163 Genoa, Italy

[5] Laboratory of NanoMedicine, Department of Cell Research and Immunology, Tel-Aviv University, Ramat Aviv, 69978 Tel-Aviv, Israel

1 Introduction

Since approximately the turn of the millennium, nanoparticles have been promoted as a paradigm-shifting approach to early diagnosis and improved treatment of multiple diseases (Ferrari 2005; Rosenblum et al. 2018). The potential of particle-based drug delivery systems, or in a simple word nanomedicines, to protect drugs (small molecules, biologicals, peptides, etc.) from premature degradation; prolong the circulation time in the blood; reduce systemic toxicity; and control release has been documented extensively by the scientific community (Shi et al. 2017). Moreover, nanomedicines enabled the realization of multifunctional delivery systems with combined therapy and diagnostics (e.g. theranostics) (Nabil et al. 2019; Arranja et al. 2017; Moore et al. 2014), co-delivery of drugs (Blanco et al.

2014; Pushpalatha et al. 2017), and targeted delivery (Tietjen et al. 2018; Lazarovits et al. 2015).

Although several nanomedicines, mostly lipid-based formulations, are under clinical investigation in early and advanced trials, there are still significant challenges in fully integrating nanomedicines into clinical practice. Some of these challenges are merely technical, such as the difficulty in the reproducible synthesis and large-scale manufacturing (Shi et al. 2017), while others are due to challenges in fundamental understanding of particle behavior in complex biological systems (Wilhelm et al. 2016; Hua et al. 2018). To this last point, a major interest in nanomedicine is understanding the transport of particles across biological barriers to their final pathological targets and critical to this goal is understanding the dynamics of particles through the extravascular tissue (Blanco et al. 2015). Researchers have attempted to overcome this grand challenge by tailoring particle physico-chemical properties (i.e. size, surface charge, surface functionalization, material density, shape, etc.), utilizing stimuli-responsive materials, masking particles in cellular coatings, using cells to shuttle particles across barriers, or employing multi-stage delivery systems. For example, Cabral et al. (2011) showed *in vivo* that particle size (30 to 100 nm) played a significant role in the accumulation of nanoparticles in tumors of varying permeability. That is, size had little effect on particle-tumor accumulation in highly permeable tumors, however when tumors have low permeability the smaller particles (30 nm) accumulate more compared to medium-sized (50 nm) or larger particles (70 and 100 nm). One approach to capitalize on these phenomena is to develop particles that modulate their size throughout their voyage to the target site. Wong et al. (2011) reported multistage nanoparticles that shrink from approximately 100 nm in diameter to 10 nm as they extravasate from the tumor vasculature into the tumor tissue. This was achieved by having a primary particle which can be actively degraded by proteases in the tumor microenvironment, thereby releasing smaller non-degraded particles (i.e. 10 nm quantum dots). In this case, the larger primary particles enable long circulation half-life and passive tumor targeting, and the release of small particles enables deeper tumor penetration. Another such multistage particle system was reported by Tasciotti et al. (2008), where larger, mesoporous silicon primary microparticles were loaded with quantum dots or single-walled carbon nanotubes (SWCNTs). This system takes advantage of the micron-sized and specifically-shaped primary particles' ability to marginate in the vasculature to better deliver the nano-sized quantum dots or SWCNTs. Finally, biomimetic approaches are attempting to utilize naturally occurring cellular processes to transport particles across biological barriers. Particles have been coated in "stealth" cellular membranes to avoid immunological detection and clearance, and improve tumor targeting (Hu et al. 2011; Pitchaimani et al. 2019). Furthermore, particles have been attached to cells as "hitchhikers" (Anselmo et al. 2015; Brenner et al. 2018) or transported across biological barriers as intracellular cargo (Choi et al. 2012; Moore et al. 2017; Zhang et al. 2018). Despite all of these innovative approaches to optimize particle transport across biological barriers, there exists a need to understand particle transport through tissues on a fundamental level.

In vivo disease models are the benchmark for studying particle transport processes as they are dynamic, complex, and mimic the biological fate of particles in human biology. However, organs-on-chips technologies are increasingly being looked at as alternatives to animal models (Sontheimer-Phelps et al. 2019). These technologies are developed with increasing complexity (i.e. able to mimic organ and organ systems), while providing precise control over the system engineering and parameters. In fact, previous studies on a simplistic collagen matrix have shown that the ionic strength of media, particle surface charge, and biophysical properties of the matrix heavily influence the diffusivity of quantum dots into a collagen gel (Stylianopoulos et al. 2010). Here, a Tissue Chamber capable of studying the diffusivity of particles through an extravascular tissue-mimic in real-time is reported. Importantly, this research aimed to show as a proof-of-principle that the Tissue Chamber chip platform could quickly evaluate particle diffusivity and observe how particle properties could be optimized to facilitate diffusion through the tissue. The Tissue Chamber was realized by fabricating a collagen gel containing a cylindrical tube throughout the center. The transport properties of small-molecule fluorescent dyes (FITC-labelled dextran with varying molecular weights), 200 nm polystyrene beads or spherical PLGA nanoparticles coated with different amounts of poly(ethylene glycol) (PEG), and liposomes coated with different molecular weight hyaluronic acids (HA) were determined through fluorescent microscopy. Image analysis was then performed to evaluate the Mean Square Displacement (MSD) and subsequently the diffusivity of these different agents. Finally, ex vivo diffusion studies were performed in freshly excised brain tissue slices.

2 Materials and methods

Materials Collagen type I (4 mg/ml) from bovine origin and dextran with different molecular weights 4, 40, and 250 kDa were purchased from Sigma Aldrich (Sigma Aldrich, USA). Dulbecco's Phosphate Buffered Saline (DPBS) was acquired from Gibco Life technologies UK and Fluoresbrite™ carboxy nyo 0.20 μm microspheres were purchased from Polysciences, Inc. (Warrington PA). Poly(lactic-co-glycolic acid) PLGA (50:50, carboxy-terminated, MW 38,000–54,000 Da) was purchased from Sigma Aldrich (St. Louis, MO, USA); 1,2-dipalmitoyl-sn-glycero-3-phosphocholine (DPPC), DSPE-PEG(2000) Carboxylic Acid, DSPE-RhB (Liss Rhod PE), DSPE-EGG, 1,2-Dipalmitoyl-*sn-glycero*-3-

phoshoethanolamine (DPPE) and cholesterol (Chol) were obtained from Avanti Polar Lipids (Alabaster, Alabama). Pure soybean phosphatidylcholine (Phospholipon 90G) (PC) was a kind gift from Phospholipid GmbH (Germany). Sodium hyaluronate was purchased from Lifecore Biomedical, LLC (MN,USA). O.C.T. mounting medium compound for cryotomy was purchased from VWR Chemicals. Permount Mounting Media was purchased from Fisher Scientific.

Synthesis of spherical polymeric nanoconstructs (SPNs) Spherical Polymeric Nanoparticles (SPNs) tagged with different amounts of PEG were prepared by a slightly modified sonication-emulsion technique according to previously described procedures (Lee et al. 2016). Two different configurations were prepared to obtain SPNs tagged with 80% or 20% of PEG on the outside surface. On both preparations, 20% of DSPE-RhB was included. Briefly, carboxyl-terminated PLGA and DPPC, in a 10:1 ratio, were dissolved in chloroform to obtain a homogeneous solution (oil phase). For the surface lipid monolayer with 80% PEG, two lipids were used (DSPE-PEG-COOH and DSPE-RhB) with a molar ratio of 5:1, dissolved in aqueous phase (4% ethanol). For the surface lipid monolayer with 20% PEG, three lipids were used (DSPE-PEG-COOH, DSPE-RhB and DSPE-EGG) with a molar ratio of 1:1:3, dissolved in aqueous phase (4% ethanol). The ratio between the oil phase and the aqueous phase was 1 to 5. Afterwards, the oil phase was added drop wisely to the aqueous phase under ultrasonication. The obtained emulsion was then placed under magnetic stirring to facilitate solvent evaporation. SPNs were centrifuged first for 5 min at 254 g to settle down any possible debris and then the supernatant was centrifuged 3 more times for 20 min at $1{,}8 \cdot 10^4$ g.

Preparation of liposomes Liposomes were synthesized according to previously published procedures (Mizrahy et al. 2014). With minor modifications, Multilamellar Vesicles (MLVs) were made by a mixture of PC, Chol and DPPE in a molar ratio of 60:20:20 (Peer and Margalit 2000; Peer and Margalit 2004; Peer et al. 2008; Kedmi et al. 2010). In brief, lipids were dissolved in ethanol, dried under reduced pressure in a rotary evaporator (Buchi Rotary Evaporator Vacuum System Flavil, Switzerland) and afterwards were hydrated using a PBS solution at pH 7.4. MLVs also contained 0.5% Cy5 labeled DPPE (Mizrahy et al. 2014). At the end, MLVs were vortexed followed by 2 h of incubation in a shaker bath at 37 °C. Then, MLVs were extruded by the use of Lipex extrusion device (Northern lipids, Vancouver, Canada) at 65 °C and under 200–500 psi nitrogen pressure. Extrusion was accomplished in several steps using decreasing pore-size polycarbonate membranes (Whatman Inc., UK), performing numerous cycles per pore-size, in order to obtain unilamellar vescicles with a size ranging between 100 and 200 nm in diameter.

Surface modifications of liposomes The liposome surface modification was made according to previous reported procedures (Landesman-Milo et al. 2013). In brief, high and low molecular weight hyaluronic acid (700 and 5 kDa, respectively) were dissolved in 0.2 M MES buffer (pH 5.5) to reach a final concentration of 5 mg/ml or 40 mg/ml. Hyaluronic Acid (HA) was activated for 30 min with ethyl-dimethyl-aminopropyl-carbodiimide (EDC) (Sigma-Aldrich, USA) and sulfo-NHS (Proteochem) using a molar ratio of 1:1:6 between HA, EDC and sulfo-NHS. Afterwards, liposomes was added and pH was adjusted to 7.4. The solution was then incubated at room temperature for 2 h and the free HA was removed by washing via centrifugation at 4 °C for 60 min at $1.3 \cdot 10^5$ g .

Size and stability characterization of nanoparticles Dynamic light scattering (DLS, Malvern Zetasizer Nano S) was employed to characterize the size and zeta (ζ) potential of nanoparticles under hydrated conditions at pH 7.0. Nanoparticle stability was performed in water at 37 °C, following the size variation through DLS measurement. The same instrument was used to determine liposomes size and ζ potential for 5 days at 37 °C using HEPES 1 M for the size and DI water for the ζ potential.

Tissue chamber fabrication The Tissue Chamber device was fabricated with polydimethylsiloxane (PDMS) using a pre-polymer solution of Sylgard 182 mixed with the curing agent in a 10:1 ratio *w*/w. This solution was poured in a petri dish to create a 3.5 mm thick PDMS sheet. The petri dish with PDMS was degassed in a vacuum chamber and cured in the oven at 60 °C overnight. After 15 min at room temperature the petri dish was cooled to −20 °C for 1 h before removing the sheet from the base. The PDMS sheets were cut into $15 \times 15 \times 3.5$ mm^3 parallelepipeds, and a $5 \times 5 \times 3.5$ mm^3 empty space for the Tissue Chamber was cut into the center. The PDMS Tissue Chamber was irreversibly bonded to a glass microscope slide (VWR) using oxygen plasma. At the end of the process, a 21 G (0.8 mm diameter) needle (Sterican B. Braun) was used to generate a channel in the Tissue Chamber from side to side. At the very end, chips were sterilized by autoclave and dried in an incubator overnight. Figure 1 illustrates the Tissue Chamber fabrication and final geometry.

Collagen type I gel preparation Collagen type I pH and ionic strength were adjusted by addition of the buffer solution (pH 7.4) to achieve a final pH between 7 and 7.4, with a final concentration of 1.5 mg/ml. 150 μl of collagen type I solution was injected inside the Tissue Chamber and polymerization occurred at 37 °C for 1 h. Next, gels were covered with 50 μl of DPBS to keep them in a hydrated state. After 1 h, the needle was removed and the channel was confirmed by optical microscope images (Fig. 1).

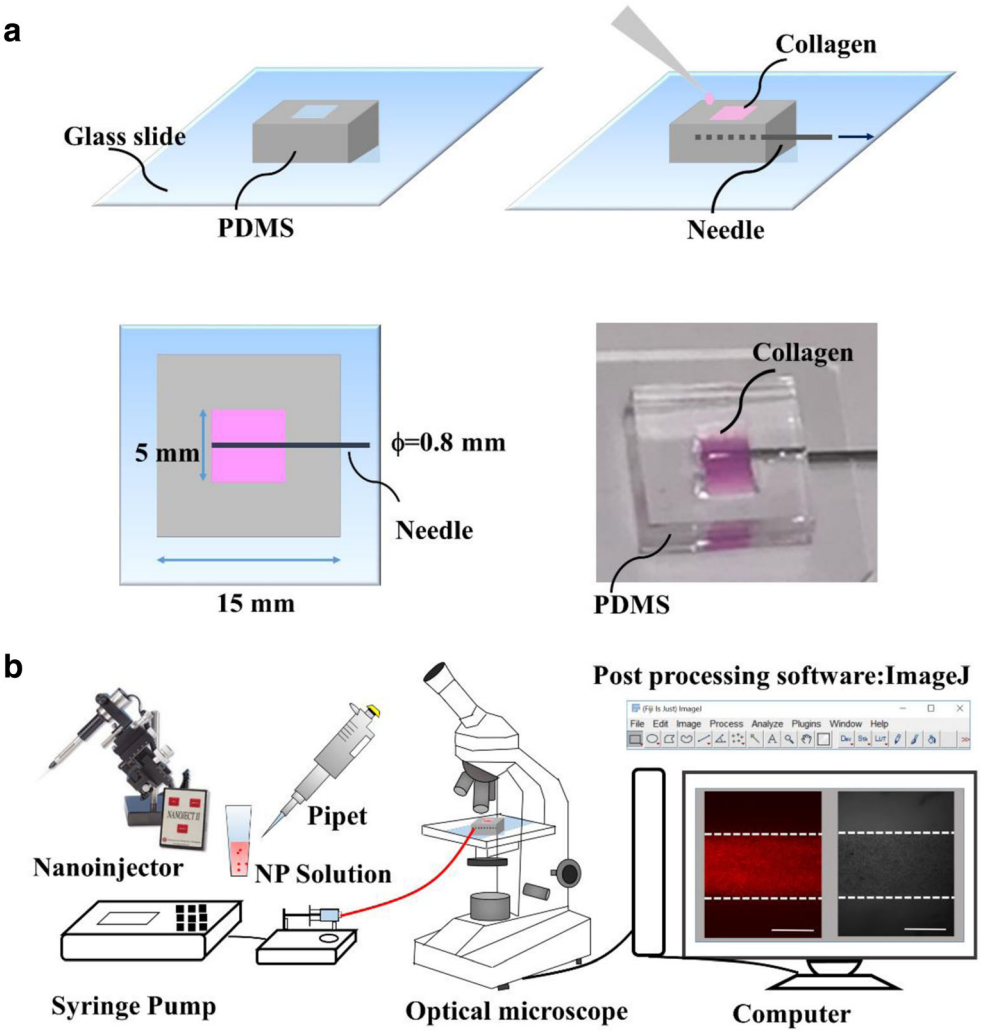

Fig. 1 Tissue Chamber microfluidic chip. a 3D schematic representation of the Tissue Chamber PDMS chip with a description of channel fabrication process, an overhead view of the Tissue Chamber showing the dimensions, and a photographic image of the Tissue Chamber bonded on a glass slide and filled with collagen type I. The photograph shows the needle inserted across the chamber, which is used to create the channel for injecting tracers. **b** Schematic of the entire experimental setup with representative optical microscopy images of 200 nm beads injected inside the channel: brightfiled (left) and fluorescent (right) images of a channel portion. Scale bars are 500 μm

Diffusion assays Samples were placed under an inverted optical microscope (Leica DMI 6000 B) equipped with a DFC360 FX digital fluorescence camera. Different molecules and particles were injected to study the diffusion through the collagen hydrogel: Dextran 4, 40 and 250 kDa, 200 nm Fluoresbrite® carboxylate microspheres, SPNs and liposomes with different PEG and HA amounts. Fluoresbrite® carboxylate microspheres (from now on called NP 200) are commercially available monodispersed fluorescent polystyrene microspheres. These microspheres were provided as a 2.5% aqueous suspensions and injected in the Tissue Chamber at 0.05% (*w*/*v*), SPNs 20% PEG and SPNs 80% PEG were injected at the same ratio (0.05% w/v). Solutions of Dextran 4, 40 and 250 kDa were injected at 0.5 mg/ml and the 3 different kinds of liposomes were injected at stock concentrations (lipid 40 mg/ml). Images were collected every 30 s for 4.5 min for the Dextran 4, 40 and 250 kDa (5 μl); every minute for 10 min in the case of NP 200; every 4 s for 44 s for all SPNs and liposomes (5 μl).

Mean square displacement (MSD) By tracking the colored wave-front inside the Tissue Chamber collagen over time, the overall diffusion coefficient D in one dimension (1D) was determined as

$$D = \frac{MSD}{2T} \tag{1}$$

where T is the time interval and the MSD were calculated from:

$$MSD_{1D} = < \Delta x(j\Delta t)^2 > \tag{2}$$

While the more general formula, for the 3D diffusion is:

$$MSD_{3D} = < \Delta x(j\Delta t)^2 + \Delta y(j\Delta t)^2 + \Delta z(j\Delta t)^2 > \tag{2a}$$

With the j index running on the total number of Δt in T and x represents the height of colored channel at time t (Valentine et al. 2004). The area of the channel perfused by the working solution is rectangular with the long edge aligned with the

800 μm injection channel and the short edge corresponding to the distance traveled by the working solution into the collagen matrix. This distance is calculated by post processing the fluorescence pics via Fiji. Notice that this distance is also the distance traveled by the molecules, or nanoparticles, over time and corresponds to the displacement in the MSD analyses. Following Xavier (2010), the MSD is calculated on all the experimental points while the diffusion coefficient is obtained by linearly interpolating the points falling in the first quartile of the MSD curves. Using the conventional formula in Eq. (1), the diffusion coefficients were determined as half of the slope of the curve fitting the MSD points in the first quartile.

Fluorescence recovery after photobleaching (FRAP) In this analysis, experiments were conducted using a Nikon A1R confocal laser scanning microscope with a Plan Apo DIC N2 20×/ 0.75 objective. A 488 nm Argon ions laser line was used to excite the samples and a bandpass 500–550 filter was placed before the photomultiplier tube. The collagen solution was placed in μ-Dish Micro-Insert 4 well (Ibidi, Germany) and 10 μl of neutralized collagen type I was polymerized at 37 °C for 1 h. Each tissue construct was injected with 23 nl using a nanoinjector (Drummond "Nanoject II" automatic nanoliter injector), following manufacturer's instructions. Injection velocity was 23 nl/s. The Nanoject II required pulled micropipets with a capillary outer diameter of 1140 μm and inner diameter of 530 μm. Experiments were performed at equilibrium, generally 12–48 h post injection depending on the MW of the molecule. Using a circular region of interest (ROI) with a radius of 92.5 μm, gels were first photobleached with a laser for 20 min and then the recovery of fluorescence was observed in the following 20 min. The recovery of fluorescence in the bleached ROIs gave the diffusion coefficient. The software provides the curve associated with bleaching and recovery as well as the parameter τ_D, which is related to the diffusion coefficient through the following formula:

$$\tau_D = \frac{\omega^2}{4D} \tag{3}$$

where ω is the radius of the ROI and D is the diffusion coefficient (Erikson et al. 2008).

Quantification of the diffusion coefficient via error minimization algorithm (EMA) This technique is useful when FRAP and MSD cannot be applied. It is rather general and robust as it takes as an input the raw data from the diffusion assays (Fig. 6). An efficient algorithm for fitting a vector of parameters on a given dataset is developed (Tröltzsch 2010). The parameters are interpreted as control variables in an optimization problem that minimizes a functional representing the difference between the experimental observations and the model predictions. The collagen gel in the Tissue Chamber chip is described as a rectangular domain Ω in which, at the initial time, a concentration $c(x,y,0)=c_{inj}(x,y)$ of molecules is prescribed. The temporal evolution of the concentration $c = c(x,y,t)$ in the time interval $[0, T]$ is described by:

$$\begin{cases} \dfrac{\partial c}{\partial t} - D\Delta c = 0 & \text{in } \Omega, t > 0, \\ D\nabla c \cdot n = 0 & \text{on } \partial\Omega \times (0,T), \\ c = c_{inj} & \text{in } \Omega, t = 0, \end{cases} \tag{4}$$

where $\Delta u = \partial_{xx}u + \partial_{yy}u$ is the Laplace operator and $c_{inj} = c_{inj}(x,y)$ is an assigned function obtained processing the fluorescence images at time $t = 0$ using the algorithm summarized in steps 1, 2, 3, 4 described in what follows. The system can be readily solved numerically if D is known (direct problem). For the inverse problem, D is not known a priori. In this case, the solution is obtained by minimizing the following functional J:

$$\min J(D) = \frac{1}{2}\left\| c(T) - \overline{c}(T) \right\|^2_{L^2(\Omega)} + \frac{\lambda}{2}|D|^2, \tag{5}$$

subject to the Eq. (4). The first term in J gives the difference between the experimentally observed concentration field $\overline{c}$ at T and the concentration field c , which is computed at time T using Eq. (4) under a specific assumption for D. The second term $\frac{\lambda}{2}|D|^2$ is a regularization operator. For the Lagrangian principle, the optimal diffusion parameter is the solution of the unconstrained minimization problem $\min \mathcal{L}(c, D, p)$ where $\mathcal{L}$ is the Lagrangian functional, defined as follows

$$\mathcal{L}(c,D,p) = J(c,D) - \int_0^T \int_\Omega \frac{\partial c}{\partial t} p - \int_0^T \int_\Omega D\nabla c \cdot \nabla p \tag{6}$$

where p is the so-called Lagrange multiplier. For the space discretization, an admissible triangulation of the domain Ω is introduced and the linear finite element method is applied (Fig. 6). For time discretization, the backward Euler scheme is chosen. To evaluate the functional J, the finite element approximation of the state equations must be compared with the observed concentration field $\overline{c}$. To this end, the pixel map of $\overline{c}$ is converted into a finite element function. This is achieved by means of image analysis tools as per the following protocol: 1. Conversion of the RGB picture for $\overline{c}$ into a gray scale image; 2. generation of a mesh with triangular elements having the same dimensions as pixel number of the image; 3. definition of a finite element variable that accounts for the grey level for each pixel; 4. projection of the previous gray scale map on a coarse mesh of triangular elements used for the solution of the finite element method applied to Eq. (4).The minimization of the Lagrangian functional is achieved by means of a Non Linear Conjugate Gradient iterative method, which, given a starting value for D, solves Eq. (4), then computes the functional J, solves for the adjoint equation to estimate p, and evaluates the derivative of $\mathcal{L}$ with respect to D. If this is sufficiently close to zero then the correct value for D

is returned. If this is not close to zero, then it updates the diffusion coefficient estimation and it runs again the full analysis starting a new iteration.

Ex vivo experiments Wild-type C57BL/6 mice aged 2–6 months were sacrificed to obtain 2.0 mm brain tissue slices via a Zivic Mouse brain slicer. The striatum of these tissues was injected with 69 nl of a solution containing approximately 1000 nanoparticles for each experiment using the nanoinjector with a velocity of 23 nl/s. Injected slices were placed in a custom-made, three-dimensional (3D) particle tracking system consisting of a wide-field inverted microscope (Nikon Ti) with an oil-immersion objective (Nikon Plan Apo VC 100×/1.4 oil DIC N2), a piezoelectric stage (Mad City Lab) and a single EMCCD camera (DU897DCS-BV Andor Technology) (Sancataldo et al. 2017; Zhang et al. 2017). Sequential images of multiple nanoparticles were recorded at 10 frames per second (fps) in time slots of 40 s (Zhang et al. 2017). At the end, the 3D particle trajectories and the corresponding MSD were calculated by post processing the movies with Fiji (Schindelin et al. 2012) and a custom MATLAB script (Supporting Information).

3 Results

The tissue chamber apparatus for the diffusion experiments The Tissue Chamber chip forms a $5 \times 5 \times 3.5$ mm^3 parallelepiped. Figure 1a shows a schematic representation of the fabrication process to realize the Tissue Chamber chip. The pink fluid is related to a collagen solution that is cast around a 21G needle (black line), which is used to realize the channel for dispersing small molecules and nanoparticles within the chip itself. The needle outer diameter is equal to 800 μm (ϕ = 0.8 mm). This size was chosen in order to ensure the mechanical stability of the channel, and thus prevent its collapse and closure. Furthermore, it should be highlighted that the overall width of the Tissue Chamber (5 mm) is significantly larger than the channel diameter (0.8 mm). This size ratio ensures that any boundary effects in the transport process can be neglected, while still realizing a working region that could be observed with a 4× objective. Fig. 1b shows the different steps in the analysis, which includes the chip fabrication; the injection of the test solution (e.g. dextran-dye or particles) via a pipette NanoInjector or syringe pump; the microscopy acquisition, and image post-processing and mathematical analysis. Specifically, in order to perform the diffusion measurements, the Tissue Chamber is placed on the stage of an inverted optical microscope, and images were acquired following the administration of fluorescent dextran or particle. Images are post-processed using Fiji (https://imagej.nih.gov/).

Analysis of the diffusion of small molecules within the tissue chamber chip In order to test the chip and the whole measurement apparatus, dextran molecules of different molecular weights were used. Specifically, 5 μl of an aqueous solution containing 4, 40 or 250 kDa FITC-dextran molecules were injected into the Tissue Chamber. The progressive spreading of the green fluorescent solution within the gel is recorded over time. The three top rows of Fig. 2a–c present the diffusing front of the dextran solutions at different time points, namely 0, 90 and 240 s. At each time point, the size of the colored area is estimated by post-processing the fluorescent images via the Fiji software. Note that the size of the channel is about 800 μm, which corresponds to the outer diameter of the needle used for realizing the channel itself within the collagen matrix. The lowest row in Fig. 2a–c shows the variation over time of the averaged MSD, calculated from the experimental data using Eq. (2) in the Methods section. Each point on these plots corresponds to the MSD at that time t, averaged over multiple experiments ($n \geq 5$). The slope of the MSD (t) curves provides, through Eq. (1), the actual diffusion coefficient. Figure 2d summarizes the experimental results providing the diffusion coefficient of the three tested molecules (4, 40 and 250 FITC-dextran) as derived from the MSD measurements in the Tissue Chamber chip (blue bars). As expected, the diffusion coefficient reduces as the molecular weight of dextran increases. For the 4 kDa dextran, a coefficient of diffusion $D = 44.20 \pm 6.65$ μm^2/s is derived. This number reduces by about 49% ($D = 22.4 \pm 16.8$ μm^2/s) for 40 kDa dextran, and by about 78% ($D = 9.9 \pm 3.71$ μm^2/s) for 250 kDa dextran.

The Einstein-Stoke relation was used to estimate the diffusion coefficients of the dextran molecules in pure water:

$$D_w = \frac{k_B T}{(6\pi\mu R_H)} \tag{7}$$

from which it results that $D_w < 270$ μm^2/s for 4 kDa dextran, < 40 μm^2/s for 40 kDa dextran, and < 20 μm^2/s for 250 kDa dextran. Indeed, as expected, the diffusion coefficient in water is significantly higher than in the collagen matrix for all dextran molecular weights. However, interestingly, it is the dextran with the smaller molecular weight (4 kDa) that is subjected to the largest reduction (6-fold) in diffusion from <270 to <45 μm^2/s. In Eq. (7), k_BT is the Boltzmann energy at room temperature ($4.11 \cdot 10^{-21}$ J), μ is the dynamic viscosity of water (10^{-3} Pa·s), and R_H is the hydrodynamic radius of the molecule ($R_H < 0.8$ nm for 4 kDa dextran, < 5 nm for 40 kDa dextran, and < 11.5 nm for 250 kDa dextran) (Armstrong et al. 2004). To validate the experimental set-up, the diffusion of dextran molecules in collagen was also assessed via Fluorescence Recovery After Photobleaching (FRAP) returning values in good agreement with those quantified within the Tissue Chamber chip. Specifically, the diffusion

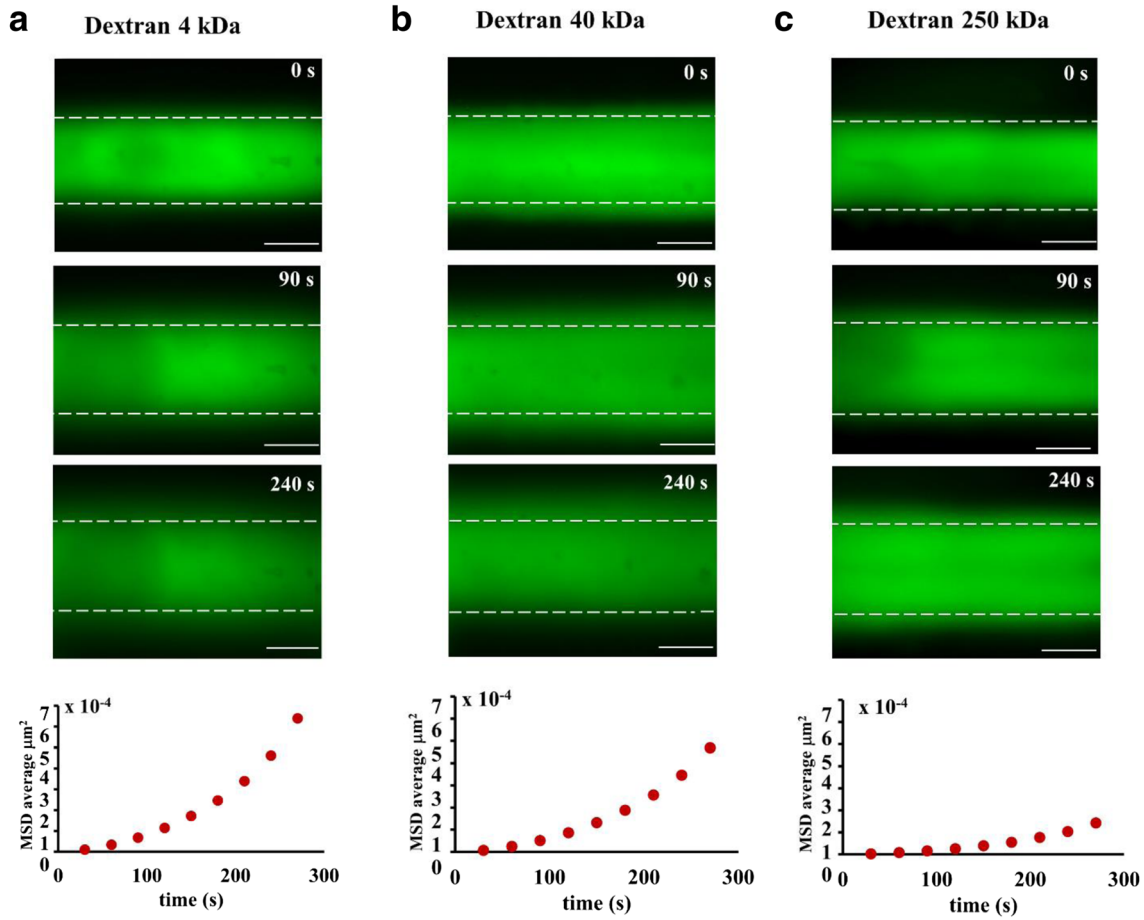

Dextran	D_{exp} (MSD) [μm²/s]	D_{exp}(FRAP) [μm²/s]	$(D_{MSD}/D_{SE})_{av}$
4 kDa	44.2±6.65	37.3±5.06	0.164
40 kDa	22.4±16.8	15.2±3.14	0.80
250 kDa	9.9±3.71	10.1±2.06	0.495

Fig. 2 Optical fluorescent microscopy images and quantification of different molecular weight Dextran diffusion. a Fluorescent images of the channel in the Tissue Chamber filled up with Dextran 4 kDa acquired at different time point (0 s, 90 s, 240 s) and averaged values of the Mean Square Displacement (MSD). **b** Fluorescent images of the channel in the Tissue Chamber filled up with Dextran 40 kDa acquired at different time point (0 s, 90 s, 240 s) and averaged values of the MSD. **c** Fluorescent images of the channel in the Tissue Chamber filled up with Dextran 250 kDa acquired at different time point (0 s, 90 s, 240 s) and averaged values of the MSD. Scale bars are 500 μm. **d** Bar chart of molecular diffusion coefficients obtained for molecules using two different analysis (MSD and Fluorescent Recovery After Photobleaching, FRAP). **e** Summarized table of MSD and FRAP derived molecular diffusion coefficients for same dye as well as their experimental and theoretical diffusion ratio. Number of repetitions $n > 5$ for MSD and $n = 4$ for FRAP. * Symbol denotes statistically significant difference $p < 0.05$, *** $p < 0.001$

coefficients estimated via FRAP were equal to $D_{FRAP} = 37.30 \pm 5.06$ μm²/s for 4 kDa dextran, 15.20 ± 3.14 μm²/s for 40 kDa dextran, and 10.10 ± 2.06 μm²/s for 250 kDa dextran. Finally, the diffusion coefficient was also estimated via the EMA approach and compared with the MSD and FRAP results. The EMA was applied using a regularization parameter $\lambda = 10^{-2}$. The diffusion coefficient was computed as the average of the diffusion coefficients resulting from the analysis of

different time intervals. In particular, $D_{EMA} = 81.15 \pm 63.09$ $\mu m^2/s$ for 4 kDa Dextran, 49.15 ± 19.73 $\mu m^2/s$ for 40 kDa Dextran and 13.54 ± 5.38 $\mu m^2/s$ for 250 kDa Dextran. Interestingly, the higher is the Dextran molecular weight, the smaller is the difference between the results obtained using the EMA and MSD.

Particle characterization In this section, the diffusion of three different nanoparticles within the collagen matrix of the Tissue Chamber chip was studied systematically. In Fig. 3, schematic representations (first row); scanning electron microscopy images (second row); and the temporal variation of size and surface ζ potential (third row) are presented for the three different nanoparticles: NP 200 – commercially available 200 nm polystyrene nanoparticles; SPN – spherical polymeric nanoparticles with all hydrodynamic diameter of approximately 200 nm; and HA-Lip – liposomes coated with a hyaluronic acid layer returning a hydrodynamic diameter around 200 nm.

The NP 200 nanoparticles have a carboxylated surface, a hydrodynamic diameter of 187.96 ± 2.42 nm and a ζ potential of -42.5 ± 2.12 mV. The stability of these particles was clearly demonstrated by the DLS data documenting a fairly constant hydrodynamic diameter over 5 days of observation (Fig. 3a, third row). The ζ potential consistently stayed between −40 and − 50 mV contributing to the electrostatic repulsion and therefore the colloidal stability of the NP 200. The electron microscopy images of Fig. 3a (second row) confirm the uniform spherical shape of these particles. The spherical polymeric nanoparticles (SPNs) were synthesized via an emulsion technique and possess a poly(lactic-co-glycolic acid) (PLGA) core stabilized by a lipid monolayer, with polyethylene glycol (PEG) chains (Lee et al. 2016; Stigliano et al. 2015). Figure 3b (first row) shows a schematic representation of SPNs documenting the polymeric/lipid structure. Chains of lipid-RhB are included in the surface monolayer thus introducing a fluorescent reporting molecules in the nanoparticle structure. Two different configurations of SPNs are realized depending

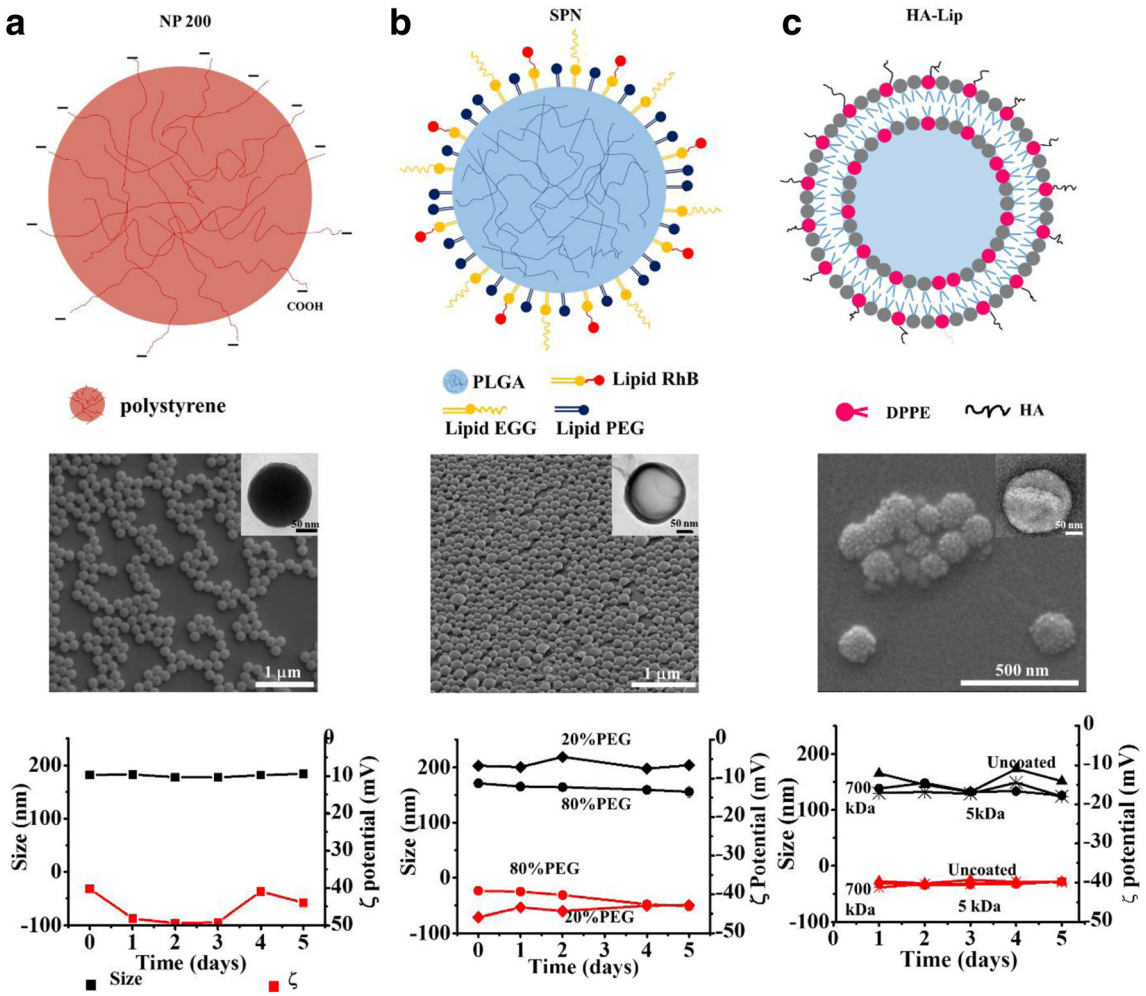

Fig. 3 Schematic representations, electron microscopy images, dynamic light scattering (DLS) hydrodynamic size and ζ-potential measurements. a Commercially available polystyrene carboxylate beads, **b** spherical PEGylated PLGA nanoparticles, and **c** liposomes coated with varying molecular weight hyaluronic acid. DLS and ζ-potential measurements were made over 5 days in water

on the initial PEG content. For 20% SPN, the initial concentration of lipid-PEG is 20% of the total lipid mass while, for 80% SPN, the initial concentration of lipid-PEG is 80% of the total lipid mass. In both cases, the electron microscopy analysis confirms the spherical shape and monodisperse size distribution of the nanoparticles (Fig. 3b, second row). At time zero, the DLS returns a hydrodynamic size of 186 ± 13 nm and a ζ potential of −45.9 ± 0.79 mV for the 20% SPNs. The 80% SPNs are slightly smaller with a hydrodynamic size of 170 ± 3 nm and a ζ potential of −39.1 ± 0.87 mV. Indeed, the higher percent of lipid-PEG on the SPN surface fosters stabilization, thus reducing the overall hydrodynamic diameter (Fig. 3c, third row). A similar behavior is observed of the HA-Lip particles. Notice that particle stabilization and size reduction have been well documented in the literature also by other authors (see for instance Essa et al. 2011; Wolfram et al. 2014). The spherical polymeric nanoconstructs are stable over the period of 5 days with an overall variation in hydrodynamic size limited to 10% for both 20% and 80% SPNs (Fig. 3c, third row).

Finally, the third type of nanoparticles schematically presented in the first row of Fig. 3c are the liposomes with an aqueous core and a lipid bilayer, which is externally coated at different degrees with hyaluronic acid (HA) (Mizrahy et al. 2014). Three different configurations of this HA-Lip are considered: liposomes not coated with any HA layer (uHA-Lip); liposomes coated with a 5 kDa HA layer (5HA-Lip); and liposomes coated with a 700 kDa HA layer (700HA-Lip). For the uHA-Lip, the initial hydrodynamic diameter was 146.1 ± 4.271 nm. This decreases to 138.5 ± 4.845 and 132.4 ± 6.493 nm for the 5HA-Lip and 700Ha-Lip, respectively. The ζ potential is stable at −37 ± 4 mV for all three configurations. SEM and TEM images confirm the DLS data. Specifically, the electron microscopy images in Fig. 3c (second row) are for the 5HA-Lip (SEM) and for uHA-Lip (TEM). Furthermore, these nanoparticles present good colloidal stability over a 5-days period Fig. 3c (third row).

Analysis of the diffusion of nanoparticles within the tissue chamber chip After confirming the size and stability of the nanoparticles, diffusion experiments were conducted in the Tissue Chamber chip. Specifically, a 5 μl solution with SPNs or HA-Lip was introduced into the chip and the progressive diffusion within the collagen matrix was recorded over time. The bar charts in Fig. 4a provides the diffusion coefficients in the collagen matrix for NP 200, the two SPN configurations, and the three HA-Lip configurations. Representative images of NP 200 in the chip, in both brightfield and fluorescence, are given in Fig. 4b. It is shown that the diffusion coefficient increases from 1.75 ± 0.65 $\mu m^2/s$ for the NP 200, un-PEGylated nanoparticles to 3.38 ± 1.89 $\mu m^2/s$ for the 20% SPNs and 4.89 ± 0.25 $\mu m^2/s$ for the 80% SPNs, which are characterized by the highest surface density of PEG. For the liposomes, the presence of HA over the surface reduces the diffusion coefficient from 5.01 ± 1.96 $\mu m^2/s$ for the uHA-Lip; to 3.83 ± 1.80 $\mu m^2/s$ for the 5HA-Lip and 2.21 ± 1.30 $\mu m^2/s$ for the 700HA-Lip. The theoretical diffusion coefficient through the equation of Einstein-Stokes was also calculated. The diffusion coefficients for the NP 200, 20% SPNs 20% PEG and SPNs 80% PEG using the EMA approach were also computed. In particular, D_{EMA} = 1.75 ± 0.65 $\mu m^2/s$ for the NP 200, 21.40 ± 7.41 $\mu m^2/s$ for the SPNs 20% PEG and 6.68 ± 2.56 $\mu m^2/s$ for the SPNs 80% PEG. While the D_{EMA} values for NP 200 and 80% SPNs are in good agreement with the MSD-derived diffusion coefficients, EMA fails in predicting accurately the diffusion for the SPNs 20% PEG.

These results emphasize that an increase in PEGylation can more efficiently lubricate the particle-tissue interface and favor the diffusion and tissue penetration (Dancy et al. 2016). For the second group of nanoparticles studied, i.e. liposomes, the diffusion coefficient within the type I collagen gel calculated with the MSD shows that the uHA-Lip diffuse more than the HA coated liposomes, ostensibly due to the interaction of collagen with hyaluronic acid (Annabi et al. 2004). Moreover, the 5HA-Lip may diffuse more than 700HA-Lip due to for their greater lubricating effect (Mizrahy et al. 2011).

Analysis of the diffusion of nanoparticles within brain tissue slices The diffusion of nanoparticles was also assessed in 2 mm thick, freshly excised brain slices from C57BL/6 wild-type mice. To avoid tissue death, brain slices were kept on ice and hydrated with cold PBS. A 69 nl of a solution containing the different types of nanoparticles was introduced in the striatum of the brain slices (Fig. 5a–c). The Nanoinjector was placed at 1.5 mm from the top of the slice and the desired volume was introduced at 0.5 mm from the bottom of the slice (Zhang et al. 2017). The dynamics of the nanoparticles was monitored over time using an inverted microscope specifically modified for single particle tracking, using an oil immersion 100× objective. Representative images are provided in Fig. 5c. The resulting movies were post-processed through the Fiji trackmate tool (Tinevez et al. 2017) and analyzed with a custom Matlab script, which was specially developed to extrapolate the MSD (Sancataldo et al. 2017; Xavier 2010). This custom MATLAB (version R2015a) script, found in the Supporting Information, was used to estimate the MSD and the diffusion coefficient of the different molecules and nanoparticles in ex vivo brain tissue.

From this analysis, 3D (x,y,z) trajectories of the individual particles over time can be extracted, as shown in Fig. 5d. Finally, the MSD of the nanoparticles can be computed and, consequently, the diffusion coefficient is derived as described in the previous paragraphs. The diffusion coefficient for the six different particles are provided by the bar chart in Fig. 5e. Notably, the trends are similar to the one derived for the same

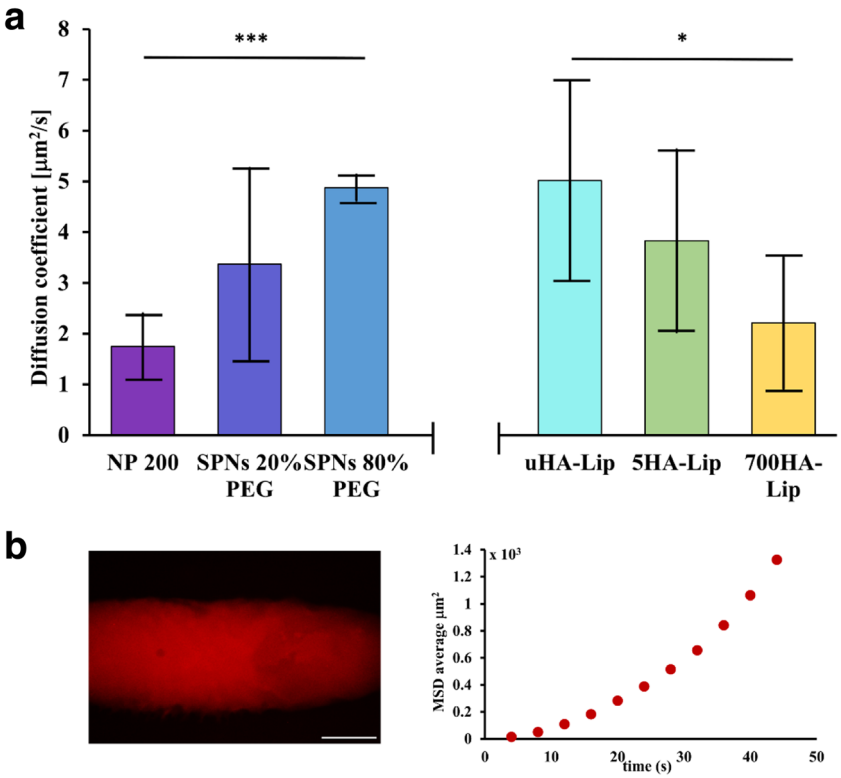

Fig. 4 Nanoparticles molecular diffusion coefficient in collagen gel. a Quantification of nanoparticles molecular diffusion coefficient in collagen gel was determined for nanoparticles using the MSD. **b** Representative fluorescent images of 5HA-Lip injected inside the Tissue Chamber and the corresponding the MSD plot. Scale bar represents 500 μm. **c** A table summarizing the nanoparticles diameters, and the MSD and Stokes-Einstein-derived molecular diffusion coefficients for the particles. $N \geq 4$. * Denotes statistically significant difference $p < 0.05$, *** $p < 0.001$

c

	Diameter (nm)	D_{MSD} [μm²/s]	D_{SE} [μm²/s]	$(D_{MSD}/D_{SE})_{av}$
NP 200	187.96±2.42	1.75±0.645	2.325	0.753
SPNs 20%PEG	186.2±13	3.38±1.89	2.347	1.440
SPNs 80%PEG	170.4±2.5	4.89±0.25	2.564	1.907
uHA-Lip	146.1 ±4.271	5.01±1.96	2.986	1.678
5HA-Lip	138.5 ±4.845	3.83±1.8	3.127	1.225
700HA-Lip	132.4 ±6.493	2.21±1.30	3.199	0.691

particle *in vitro* within the collagen matrix of the Tissue Chamber chip. In other words, the diffusion coefficient increase moving from un-PEGylated nanoparticles (NP 200) to PEGylated SPNs, and reduces with the presence of HA on liposomes. Specifically, the diffusion was $2.68 \pm 1.33 \cdot 10^{-5}$ μm²/s for the NP 200; $4.84 \pm 2.41 \cdot 10^{-5}$ μm²/s for the 20% SPNs; $5.36 \pm 2.49 \cdot 10^{-5}$ μm²/s for the 80% SPNs; $6.32 \pm 2.81 \cdot 10^{-5}$ μm²/s for the uHA-Lip; $3.50 \pm 1.91 \cdot 10^{-5}$ μm²/s for the 5HA-Lip; and $2.48 \pm 1.35 \cdot 10^{-5}$ μm²/s for the 700HA-Lip.

Comparing these results with the one obtained in the Tissue Chamber chip, a decrease in the diffusion coefficient of five orders of magnitude was noticed. This is indeed expected given that the Tissue Chamber chip does not include cells in its current configuration.

4 Discussion

Here, a Tissue Chamber chip has been demonstrated for estimating the diffusion ability of nanoparticles under controlled biophysical conditions. First, the diffusion of FITC-Dextran molecules with three different molecular weights (4, 40 and 250 kDa) was assessed in a collagen gel using two different and independent techniques. The first approach is based on extracting the diffusion coefficient from the Mean Square Displacement (MSD). This is a very general technique that can be applied to molecules and nanoparticles. The second approach is based on the use of Fluorescence recovery After Photo-bleaching (FRAP), but this technique cannot be applied to nanoparticles. Figure 2d shows that the diffusion coefficients estimated with both techniques are in

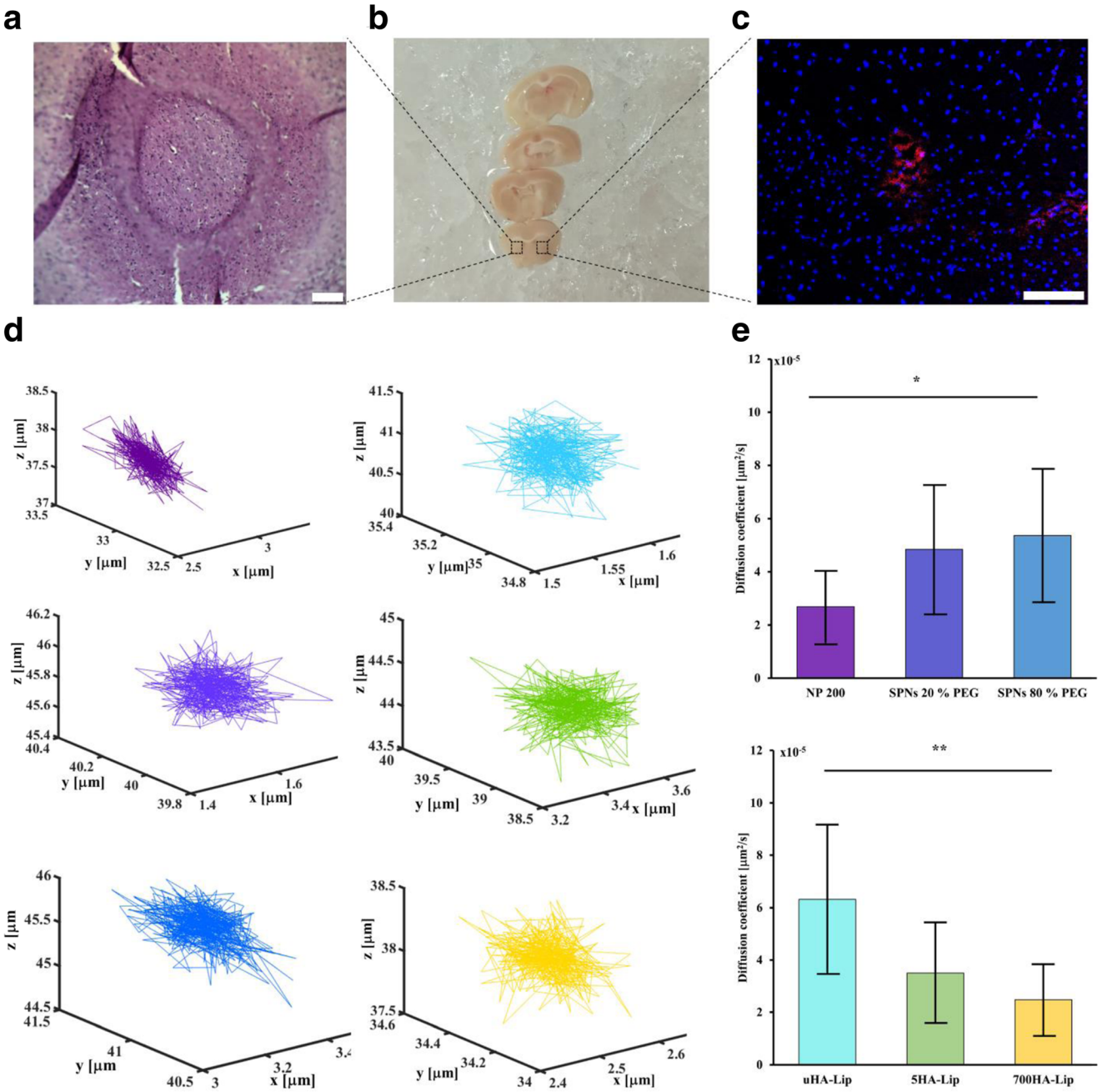

Fig. 5 Ex-vivo single tracking and quantification of nanoparticles molecular diffusion coefficient. **a** Representative image of a 12 µm mouse brain slice stained with H&E with recognizable sign of the injection needle. Scale bar represents100 µm. **b** Representative image of different brain sections. Squares highlight the striatum. **c** Confocal fluorescent microscopy image of a brain slice shows the NPs as red spots and the nuclei stained in DAPI. Scale bar represents 100 µm. **d** 3D trajectories of the particles diffusing through ex vivo brain slices. **e** Diffusion coefficients obtained for nanoparticles in the ex vivo brain tissue derived using MSD analysis. * Denotes a statistically significant difference $p < 0.05$, ** $p < 0.01$

good agreement and no statistically significant difference is documented for all three tested Dextran molecules ($p = 0.118$ for 4 kDa dextran; $p = 0.426$ for 40 kDa dextran; and $p = 0.926$ for 250 kDa dextran). The FRAP technique is easier and more reliable then the MSD approach, as suggested by the smaller variations among the different measurements. The MSD technique is more cumbersome and reproducibility is more affected by the intrinsic higher difficulty associated with performing the experiments. Specifically, the channel diameter may vary slightly between experiments due to the fabrication process, the connection with external tubing or pipettes to the channel is not always optimal, and so on. Yet, FRAP and MSD return values for the diffusion coefficient that are in close

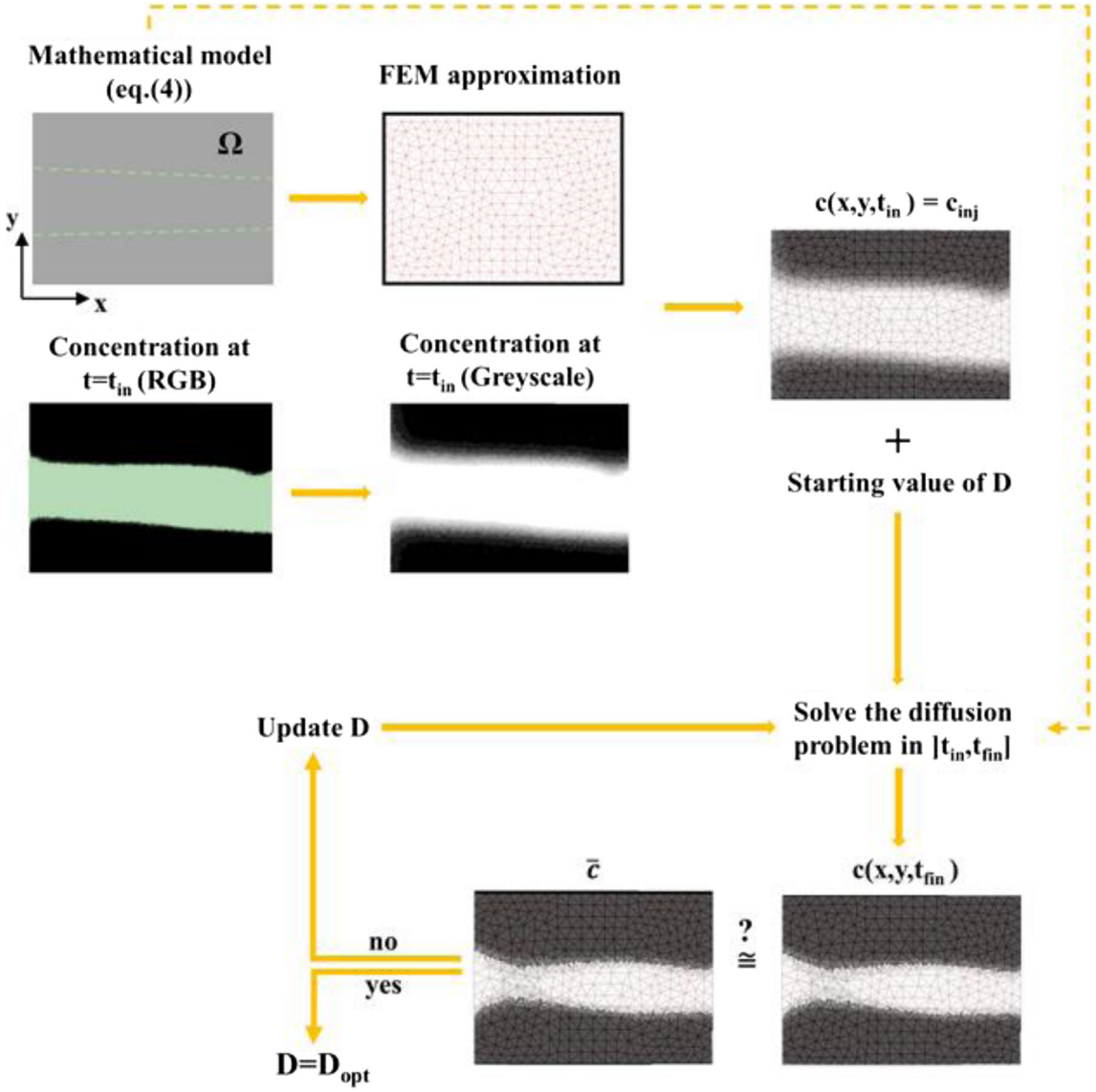

Fig. 6 Quantification of the diffusion coefficient via an error minimization algorithm. Post-processing of the experimental data with conversion of the fluorescent microscopy images into greyscale maps and error minimization procedure implemented in the computational algorithm

agreement. This demonstrates the accuracy and reliability of the whole measurement protocol and the Tissue Chamber chip.

As FRAP cannot be applied to nanoparticles, the following measurements on SPNs and HA-Lip particles were performed using the MSD (Fig. 4) and EMA (Fig. 6) approaches. Figure 4 shows that the decoration of the nanoparticle surface with short PEG chains (2 kDa) increases their diffusivity in the collagen gel. This trend is indeed in agreement with the experimental results presented by Zhang et al. (2017). In their work, the diffusion of two nanoparticles (65 ± 3 nm bare cisplatin-loaded poly(aspartic acid) (PAA) particles and 74 ± 2 nm PEGylated cisplatin-loaded PAA particles) was assessed within freshly excised healthy rat brain tissue slices. Under these conditions, Zhang and colleagues derived diffusion coefficients of the order of 10^{-3} $\mu m^2/s$ and 10^{-1} $\mu m^2/s$ for naked and PEGylated particles, respectively. Other authors have estimated the diffusion of PEGylate particles into mucus (Cu and Saltzman 2009; Xu et al. 2015). Even in these works, the addition of PEG chains over a PLGA particle core improved diffusion. This was mainly ascribed to steric interactions arising at the interface between PEG chains and the surrounding mucus structure. More recently, Labouta et al. (2018) showed that PEG density was the contributing factor in determining the penetration depth of liposome into collagen gels. Similarly, in this work the coating of spherical, solid polymeric nanoparticles with PEG (2 kDa) increases the mobility within the collagen gel, as compared to bare nanoparticles.

Following the same procedure of Zhang and colleagues, the diffusion of bare and PEGylated nanoparticles was also

assessed in freshly excised brain tissue slides. The same behavior observed for the *in vitro* experiments were also documented ex vivo. Specifically, the nanoparticle diffusion increases with the surface density of the PEG chains. Indeed, the absolute values of the ex vivo diffusion coefficient are significantly smaller than those documented *in vitro*. This difference should be mostly attributed to three differences between the excised brain tissue and the Tissue Chamber chip, namely the presence of cells, the extracellular matrix composition, and the limited extracellular space that characterizes brain tissues (Syková and Nicholson 2008). It should be emphasized that it is difficult to perform a direct and objective comparison with previous results available in the literature because of differences in particle size and surface properties. Thorne and Nicholson (2006) measured, in living animals, the diffusivity of 35 nm quantum dots to be in the order of 10^{-1} $\mu m^2/s$. Zhang and colleagues (Zhang et al. 2017) measured the diffusivity of 60 nm PAA particles to be in the order of 10^{-3} to 10^{-1} $\mu m^2/s$. In the current manuscript, the authors estimated the diffusivity of 200 nm particles to be in the order of 10^{-5} to 10^{-4} $\mu m^2/s$. These significant differences in diffusivity could be also ascribed to the significant difference in particle size.

In the case of hyaluronic acid-functionalized liposomes, the opposite trend was observed. Specifically, HA decoration over the liposome surface was responsible for a significant reduction in mobility. This decrease was directly related to HA molecular weight and possibly due to the entanglement of the long HA chains with the surrounding extracellular matrix. This macromolecular phenomenon may be driven by electrostatic forces (Gelman and Blackwell 1974) or by specific HA-collagen interactions (Annabi et al. 2004; McDevitt et al. 1991). Importantly, even in the case of the HA-Lip, the *in vitro* trends are in full agreement with the ex vivo observations.

5 Conclusions

Taken all together, the data presented in this manuscript show that the proposed Tissue Chamber chip provides a versatile platform that can realize fundamental studies on particle diffusion in a tissue-like environment. Importantly, multiple biophysical parameters can be accurately controlled. For example, the tissue composition can be tailored to include collagen type I, type IV as well as hyaluronic acid, matrigel, other biomacromolecules, and combinations thereof. Furthermore, the ECM can be modified to express specific adhesion molecules (e.g. integrins) or the density can be modified to affect the porosity of the tissue. Finally, cells could be included which could dynamically remodel the ECM, interact with the particles (uptake and trafficking) or act as physical barriers to particle transport. This platform can therefore be employed to conduct systematic, comparative studies to evaluate nanoparticle transport processes in different recapitulated tissues. With such a tool it would be possible to optimize the geometrical and surface properties of nanoparticles to achieve high and uniform tissue penetration.

Acknowledgments All the authors have read and approved the manuscript. This project was partially supported by the European Research Council, under the European Union's Seventh Framework Programme (FP7/2007-2013)/ERC grant agreement no. 616695, by the Italian Association for Cancer Research (AIRC) under the individual investigator grant no. 17664, and by the European Union's Horizon 2020 research and innovation programme under the Marie Skłodowska-Curie grant agreement no. 754490.

References

B. Annabi, S. Thibeault, R. Moumdjian, R. Béliveau, J. Biol. Chem. **279**, 21888 (2004)
A.C. Anselmo, J.B. Gilbert, S. Kumar, V. Gupta, R.E. Cohen, M.F. Rubner, S. Mitragotri, J. Control. Release **199**, 29 (2015)
J.K. Armstrong, R.B. Wenby, H.J. Meiselman, T.C. Fisher, Biophys. J. **87**, 4259 (2004)
A.G. Arranja, V. Pathak, T. Lammers, Y. Shi, Pharmacol. Res. **115**, 87 (2017)
E. Blanco, T. Sangai, S. Wu, A. Hsiao, G.U. Ruiz-Esparza, C.A. Gonzalez-Delgado, F.E. Cara, S. Granados-Principal, K.W. Evans, A. Akcakanat, Y. Wang, K.A. Do, F. Meric-Bernstam, M. Ferrari, Mol. Ther. **22**, 1310 (2014)
E. Blanco, H. Shen, M. Ferrari, Nat. Biotechnol. **33**, 941 (2015)
J.S. Brenner, D.C. Pan, J.W. Myerson, O.A. Marcos-Contreras, C.H. Villa, P. Patel, H. Hekierski, S. Chatterjee, J.-Q. Tao, H. Parhiz, K. Bhamidipati, T.G. Uhler, E.D. Hood, R.Y. Kiseleva, V.S. Shuvaev, T. Shuvaeva, M. Khoshnejad, I. Johnston, J.V. Gregory, J. Lahann, T. Wang, E. Cantu, W.M. Armstead, S. Mitragotri, V. Muzykantov, Nat. Commun. **9**, 2684 (2018)
H. Cabral, Y. Matsumoto, K. Mizuno, Q. Chen, M. Murakami, M. Kimura, Y. Tereda, M.R. Kano, K. Miyazono, M. Uesaka, N. Nishiyama, K. Kataoka, Nat. Nanotechnol. **6**, 815 (2011)
M.-R. Choi, R. Bardhan, K.J. Stanton-Maxey, S. Badve, H. Nakshatri, K.M. Stantz, N. Cao, N.J. Halas, S.E. Clare, Cancer Nanotechnol. **3**, 47 (2012)
Y. Cu, W.M. Saltzman, Mol. Pharm. **6**, 173 (2009)
J.G. Dancy, A.S. Wadajkar, C.S. Schneider, J.R.H. Mauban, O.G. Goloubeva, G.F. Woodworth, J.A. Winkles, A.J. Kim, J. Control. Release **238**, 139 (2016)
A. Erikson, H.N. Andersen, S.N. Naess, P. Sikorski, C.d.L. Davies, Biopolymers **89**, 135 (2008)
S. Essa, J.M. Rabanel, P. Hildgen, Int. J. Pharm. **411**, 178 (2011)
M. Ferrari, Nat. Rev. Cancer **5**, 161 (2005)
R.A. Gelman, J. Blackwell, Biochim. Biophys. Acta **342**, 254 (1974)
C.-M.J. Hu, L. Zhang, S. Aryal, C. Cheung, R.H. Fang, L. Zhang, Proc. Natl. Acad. Sci. **108**, 10980 (2011)
S. Hua, M.B.C. de Matos, J.M. Metselaar, G. Storm, Front. Pharmacol. **9**, 790 (2018)
R. Kedmi, N. Ben-Arie, D. Peer, Biomaterials **31**, 6867 (2010)
H.I. Labouta, M.J. Gomez-Garcia, C.D. Sarsons, T. Nguyen, J. Kennard, W. Ngo, K. Terefe, N. Iragorri, P. Lai, K.D. Rinker, D. Cramb, RSC Adv. **8**, 7697 (2018)

D. Landesman-Milo, M. Goldsmith, S. Leviatan-Ben-Arye, B. Witenberg, E. Brown, S. Leibovitch, S. Azriel, S. Tabak, V. Morad, D. Peer, Cancer Lett. **334**, 221 (2013)
J. Lazarovits, Y.Y. Chen, E.A. Sykes, W.C.W. Chan, Chem. Commun. **51**, 2756 (2015)
A. Lee, D. di Mascolo, M. Francardi, F. Piccardi, T. Bandiera, P. Decuzzi, Nanomed.: Nanotechnol. Biol. Med. **12**, 2139 (2016)
C.A. McDevitt, J. Marcelino, L. Tucker, FEBS Lett. **294**, 167 (1991)
S. Mizrahy, S.R. Raz, M. Hasgaard, H. Liu, N. Soffer-Tsur, K. Cohen, R. Dvash, D. Landsman-Milo, M.G.E.G. Bremer, S.M. Moghimi, D. Peer, J. Control. Release **156**, 231 (2011)
S. Mizrahy, M. Goldsmith, S. Leviatan-Ben-Arye, E. Kisin-Finfer, O. Redy, S. Srinivasan, D. Shabat, B. Godin, D. Peer, Nanoscale **6**, 3742 (2014)
T.L. Moore, H. Chen, R. Morrison, F. Wang, J.N. Anker, F. Alexis, Mol. Pharm. **11**, 24 (2014)
T.L. Moore, D. Hauser, T. Gruber, B. Rothen-Rutishauser, M. Lattuada, A. Petri-Fink, R. Lyck, ACS Appl. Mater. Interfaces **9**, 18501 (2017)
G. Nabil, K. Bhise, S. Sau, M. Atef, H.A. El-Banna, A. Iyer, Drug Discov. Today **24**, 462 (2019)
D. Peer, R. Margalit, Arch. Biochem. Biophys. **383**, 185 (2000)
D. Peer, R. Margalit, Int. J. Cancer **108**, 780 (2004)
D. Peer, E.J. Park, Y. Morishita, C.V. Carman, M. Shimaoka, Science **319**, 627 (2008)
A. Pitchaimani, T.D.T. Nguyen, R. Marasini, A. Eliyapura, T. Azizi, M. Jaberi-Douraki, S. Aryal, Adv. Funct. Mater. **29**, 1806817 (2019)
R. Pushpalatha, S. Selvamuthukumar, D. Kilimozhi, J. Drug Delivery Sci. Technol. **39**, 362 (2017)
D. Rosenblum, N. Joshi, W. Tao, J.M. Karp, D. Peer, Nat. Commun. **9**, 1410 (2018)
G. Sancataldo, L. Scipioni, T. Ravasenga, L. Lanzanò, A. Diaspro, A. Barberis, M. Duocastella, Optica **4**, 367 (2017)
J. Schindelin, I. Arganda-Carreras, E. Frise, V. Kaynig, M. Longair, T. Pietzsch, S. Preibisch, C. Rueden, S. Saalfeld, B. Schmid, J.Y. Tinevez, D.J. White, V. Hartenstein, K. Eliceiri, P. Tomancak, A. Cardona, Nat. Methods **9**, 676 (2012)
J. Shi, P.W. Kantoff, R. Wooster, O.C. Farokhzad, Nat. Rev. Cancer **17**, 20 (2017)
A. Sontheimer-Phelps, B.A. Hassell, D.E. Ingber, Nat. Rev. Cancer **19**, 65 (2019)
C. Stigliano, J. Key, M. Ramirez, S. Aryal, P. Decuzzi, Adv. Funct. Mater. **25**, 3371 (2015)
T. Stylianopoulos, M.-Z. Poh, N. Insin, M.G. Bawendi, D. Fukumara, L.L. Munn, R.K. Jain, Biophys. J. **99**, 1342 (2010)
E. Syková, C. Nicholson, Physiol. Rev. **88**, 1277 (2008)
E. Tasciotti, X. Liu, R. Bhavane, K. Plant, A.D. Leonard, B.K. Price, M.M.-C. Cheng, P. Decuzzi, J.M. Tour, F. Robertson, M. Ferrari, Nat. Nanotechnol. **3**, 151 (2008)
R.G. Thorne, C. Nicholson, Proc. Natl. Acad. Sci. **103**, 5567 (2006)
G.T. Tietjen, L.G. Bracaglia, W.M. Saltzman, J.S. Pober, Trends Mol. Med. **24**, 598 (2018)
J.-Y. Tinevez, N. Perry, J. Schindelin, G.M. Hoopes, G.D. Reynolds, E. Laplantine, S.Y. Bednarek, S.L. Shorte, K.W. Eliceiri, Methods **115**, 80 (2017)
F. Tröltzsch, Optimal control of partial differential equations, vol. 112 (Graduate Studies in Mathematics, 2010)
M.T. Valentine, Z. E: Perlman, M.L. Gardel, J.H. Shin, P. Matsudaira, T.J. Mitchison, D.A. Weitz, Biophys. J. **86**, 4004 (2004)
S. Wilhelm, A.J. Tavares, Q. Dai, S. Ohta, J. Audet, H.F. Dvorak, W.C.W. Chan, Nat. Rev. Mater. **1**, 16014 (2016)
J. Wolfram, K. Suri, Y. Yang, J. Shen, C. Celia, M. Fresta, Y. Zhao, H. Shen, M. Ferrari, Colloid Surf. B Biointerfaces **114**, 294 (2014)
C. Wong, T. Stylianopoulos, J. Cui, J. Martin, V.P. Chauhan, W. Jiang, Z. Popović, R.K. Jain, M.G. Bawendi, D. Fukumura, Proc. Natl. Acad. Sci. **108**, 2426 (2011)
M. Xavier, Phys. Rev. **E82**, 041914 (2010)
Q. Xu, L.M. Ensign, N.J. Boylan, A. Schön, X. Gong, J.-C. Yang, N.W. Lamb, S. Cai, T. Yu, E. Freire, J. Hanes, ACS Nano **9**, 9217 (2015)
C. Zhang, E.A. Nance, P. Mastorakos, J. Chisholm, S. Berry, C. Eberhart, B. Tyler, H. Brem, J.S. Suk, J. Hanes, J. Control. Release **263**, 112 (2017)
W. Zhang, M. Wang, W. Tang, R. Wen, S. Zhou, C. Lee, H. Wang, W. Jiang, I.M. Delahunty, Z. Zhen, H. Chen, M. Chapman, Z. Wu, E.W. Howerth, H. Cai, Z. Li, J. Xie, Adv. Mater. **30**, 1805557 (2018)